GEOFLUIDS

Geofluids (2016) **16**, 452–463 doi: 10.1111/gfl.12165

Modeling earthquake effects on groundwater levels: evidences from the 2012 Emilia earthquake (Italy)

M. NESPOLI[1,2], M. TODESCO[1], E. SERPELLONI[3], M. E. BELARDINELLI[2], M. BONAFEDE[2], M. MARCACCIO[4], A. P. RINALDI[5], L. ANDERLINI[1,2] AND A. GUALANDI[1,2]

[1]Sezione di Bologna, Istituto Nazionale di Geofisica e Vulcanologia, Bologna, Italy; [2]Università degli Studi di Bologna, Bologna, Italy; [3]Centro Nazionale Terremoti, Istituto Nazionale di Geofisica e Vulcanologia, Bologna, Italy; [4]Agenzia Regionale Prevenzione e Ambiente (ARPA) dell'Emilia-Romagna, Direzione Tecnica, Bologna, Italy; [5]Swiss Seismological Service, ETH Zürich, Zürich, Switzerland

ABSTRACT

Changes in water level are commonly reported in regions struck by a seismic event. The sign and amplitude of such changes depend on the relative position of measuring points with respect to the hypocenter, and on the poroelastic properties of the rock. We apply a porous media flow model (TOUGH2) to describe groundwater flow and water-level changes associated with the first M_L5.9 mainshock of the 2012 seismic sequence in Emilia (Italy). We represent the earthquake as an instantaneous pressure step, whose amplitude was inferred from the properties of the seismic source inverted from geodetic data. The results are consistent with the evolution recorded in both deep and shallow water wells in the area and suggest that our description of the seismic event is suitable to capture both timing and magnitude of water-level changes. We draw some conclusions about the influence of material heterogeneity on the pore pressure evolution, and we show that to reproduce the observed maximum amplitude it is necessary to take into account compaction in the shallow layer.

Key words: 2012 Emilia earthquake, groundwaters, isotropic stress, permeability, porosity, water wells

Received 23 June 2015; accepted 22 October 2015

Corresponding author: Massimo Nespoli, Sezione di Bologna, Istituto Nazionale di Geofisica e Vulcanologia, Bologna 40128, Italy. Email: massimo.nespoli@ingv.it. Tel: +39 0514151483. Fax: +39 0514151499.

Geofluids (2016) **16**, 452–463

INTRODUCTION

Earthquakes are known to affect groundwater: this occurs when seismicity acts on saturated porous rocks, and the stress change is transferred from the solid grain to the interstitial fluids (Roeloffs 1998; Ge & Stover 2000; Manga & Wang 2007). The seismic event then alters the distribution of the pore pressure within the aquifer, causing changes in water level and changes in the discharge of streams, springs, or geysers. Coseismic stress changes affect both the magnitude and the sign of the water-level changes: here we assume that a negative stress change leads to rock compression, and hence to pore pressure increase, whereas positive stress changes, and the related rock expansion, lead to a pore pressure drop. When the seismically induced pressure gradients cause the mixing of different water bodies, changes of aquifer composition and temperature may also be recorded (Wang & Manga 2010 and refs. therein). The aquifer poroelastic response to seismicity can extend to the postseismic phase as shown in Iceland, where fluid set in motion by the earthquake drove transient deformation that was recorded by geodetic measurements and lasted a few months (Jónsson *et al.* 2003). Long-term effects can also be associated with permanent or transient changes in the properties of the rock, which may undergo undrained contraction, liquefaction, or changes (both positive or negative) in porosity and permeability (Elkhoury *et al.* 2006; Manga & Brodsky 2006; Manga *et al.* 2009, 2012; Shi *et al.* 2014).

The observed hydrological changes reflect the coupling between mechanical and fluid-dynamic processes within the crust. Such coupling operates in both ways, as the presence of fluids within the crust may itself trigger seismicity (Ellsworth 2013; Grünthal 2013; and ref. therein) and drive the evolution of aftershock sequences (Miller *et al.* 2004): the fluid pressure modifies the effective normal stress; therefore, a pore pressure increase may favor the onset of seismicity, whereas a pressure drop may hinder it. Understanding the extent and functioning of this hydro-mechanical coupling is therefore useful for a proper assessment of

seismic hazard and has implications for all the industrial activities that involve massive fluid injection or withdrawal and the related growing concerns about the risk of induced seismicity. Several authors have focused on the coseismic well response to static strain (Roeloffs 1996; Roeloffs & Quilty 1996; Grecksch *et al.* 1999; Ge & Stover 2000; Jónsson *et al.* 2003; Shi *et al.* 2014) and explored dynamic effects associated with the passage of seismic waves (Roeloffs 1998; Brodsky *et al.* 2003; Elkhoury *et al.* 2006; Wang & Chia 2008; Wang *et al.* 2009; Shi *et al.* 2014; Weingarten & Ge 2014). The hydrological effects of both static and dynamic stress changes are known to depend on magnitude and distance of the triggering earthquake (Wang & Manga 2010; and refs. therein): in the near field (i.e., within a distance comparable to the size of the rupture along the fault), static and peak dynamic stress changes have a comparable magnitude, whereas in the far field (more than several times the size of the ruptured fault) permeability changes due to dynamic strain seem to control hydrological effects (Wang & Manga 2010).

Focusing on the near field, some studies describe observed changes in water level and its temporal evolution based on the coseismic static stress field (Ge & Stover 2000; Jónsson *et al.* 2003). In this approach, the static stress change is used to compute the coseismic pore pressure variation; its temporal evolution is then computed according to a diffusion equation over a homogeneous and uniform half-space (Ge & Stover 2000). These results provided interesting insights on the hydro-mechanical coupling, although the details of the groundwater response cannot be entirely captured.

In the present work, we take into account the effects of heterogeneous rock properties and the presence of an unsaturated region. The use of a multiphase, multicomponent porous flow model (TOUGH2, Pruess *et al.* 2012) allows us to track the groundwater flow and its temporal evolution within both confined and unconfined aquifers, accounting for the local geothermal gradient and for potential temperature changes associated with fluid migration. Following the approach described above, the effect of seismicity is represented as an instantaneous pore pressure change estimated from the static, coseismic, strain field. The simulated effects on water level were tested against field data. Our case history is the seismic sequence that struck the plain of the Po river (northern Italy) in 2012 (Fig. 1), for which hourly data on water level in monitored wells are available and display remarkable changes in the near field (Fig. 2). Here we provide information on both the seismic sequence and the observed water-level changes, and present the results of numerical simulations. The first set of simulations focuses on the role of heterogeneity in controlling the aquifer response. We then evaluate the effects of compaction.

The results show that:

(1) Our representation of seismicity (i.e., the coseismic deformation) within the groundwater model is adequate and provides a satisfactory description of the observed water-level changes.
(2) Heterogeneous rock properties control the different response observed at different wells.
(3) The details of the postseismic water-level evolution in shallow wells are better captured if the effects of rainfall and compaction are included.

THE 2012 EMILIA SEISMIC SEQUENCE AND WATER WELL RESPONSE

The seismic sequence that struck the Po Plain, Northern Italy, in 2012 (Fig. 1), featured two main events: the first, on May 20 (4:04 AM, local time) with a magnitude $M_L = 5.9$, occurred near Finale Emilia at a depth of 6.3 km; the second took place on May 29 (9:00 AM, local

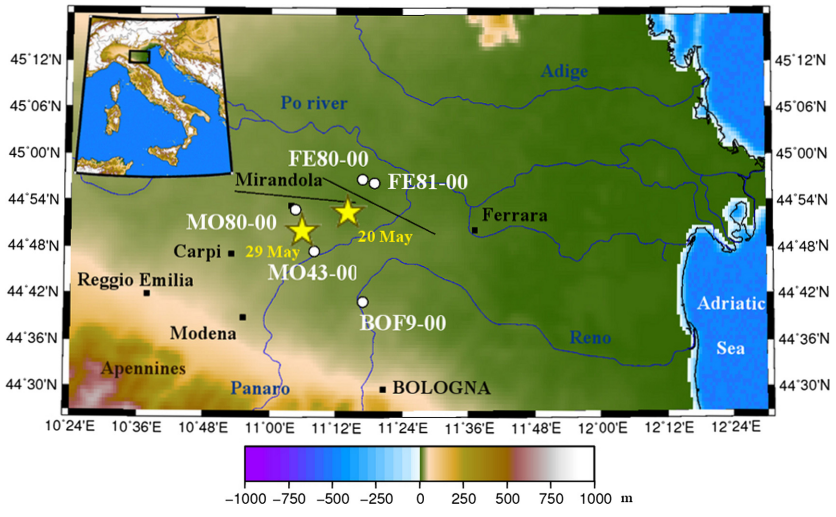

Fig. 1. Map of the study area. White dots represent five water wells considered in this work; stars represent epicenters of two mainshocks of the 2012 Emilia seismic sequence; black lines represent the fault traces for the May 20 (northeast) and May 29 (to the west) events (Pezzo *et al.* 2013).

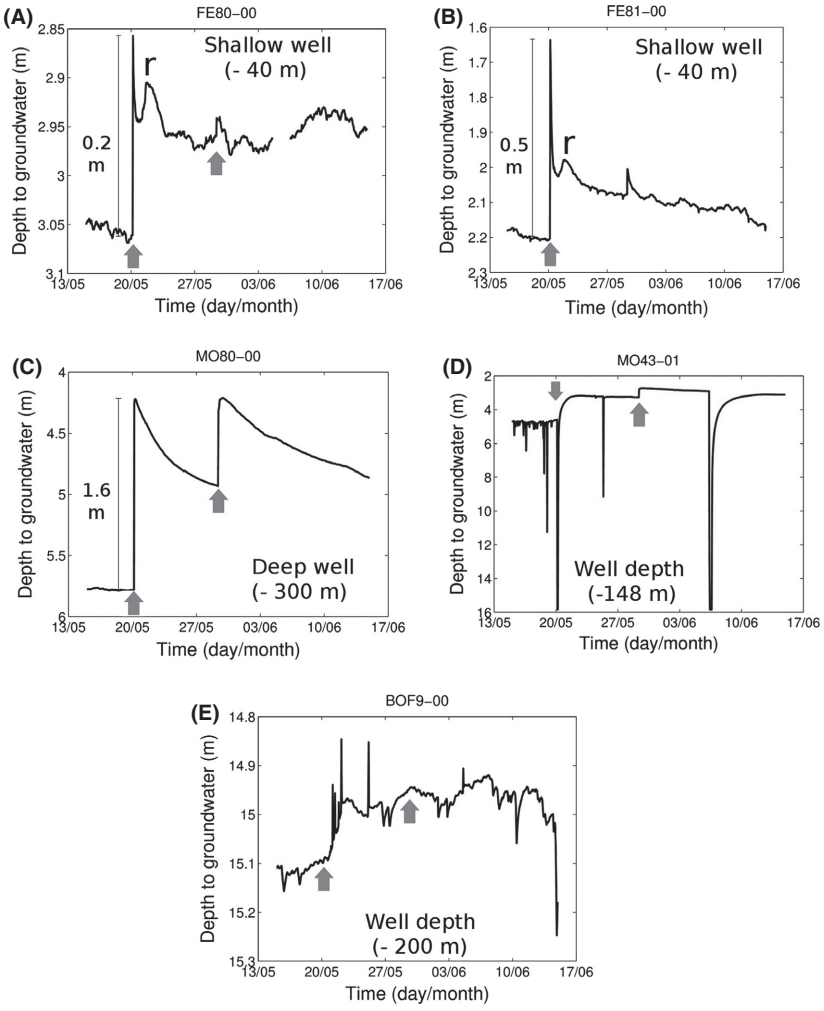

Fig. 2. (A, E) Observed water-level changes at different wells. Gray arrows indicate the events of May 20 and May 29, 2012. Note minor water-level rise ('*r*' in Fig. 2A,B) shortly after the first mainshock, in the shallow wells only.

time), 15 km southwest of the first event, near Mirandola, at a depth of 10.2 km and a magnitude $M_L = 5.8$ (Scognamiglio *et al.* 2012). Here we focus on the aquifer response to the May 20 event. The coseismic slip associated with this event was inferred by various authors based on seismic and geodetic data (Serpelloni *et al.* 2012; Cesca *et al.* 2013; Pezzo *et al.* 2013). Here we consider the results by Pezzo *et al.* (2013), who performed a nonlinear inversion of InSAR and GPS data, assuming dislocation in an elastic half-space, and a fault geometry constrained by geological and geophysical data. The resulting coseismic slip is distributed along a fault model that has a surface trace of 34 km, a strike of 114, and a rake of 90° (Fig. 3). According to Pezzo *et al.* (2013), the dip of the fault changes with depth, with a shallow and steeper portion (dipping 40° SSW) that extends 11 km along dip, and a deeper and more gently dipping sector (20° SSW) that extends 12 km along dip. The coseismic slip, however, mostly occur on the upper portion of the fault, reaching a maximum value of 120 cm near its center (Fig. 3).

The groundwater response to the seismic sequence was captured by the monitoring network of the regional agency for environmental protection (ARPA). The network consists of 40 instrumented water wells (Fig. S1, Table S1), evenly distributed across the region, that probe aquifers at different depths and provide hourly data on temperature, electrical conductivity and water level (Marcaccio & Martinelli 2012. Only five wells, close to the epicentral area (Fig. 1), recorded significant water-level changes after the earthquake, suggesting that the seismic effects on the groundwater system are local. We cannot exclude far-field effects, sometime associated with dynamic strain, owing to the low sampling rate (1 h^{-1}) in these wells. In this area, the Po Plain is characterized by fine deposits that form superimposed, confined aquifers, while phreatic aquifers, sensitive to meteoric recharge, are only present at shallow depths (tens of m). The five wells that responded to the seismic events reach different depths (from −40 to −300 m) and all experienced a water-level rise (Fig. 2). No well in the entire network recorded a water-level drop

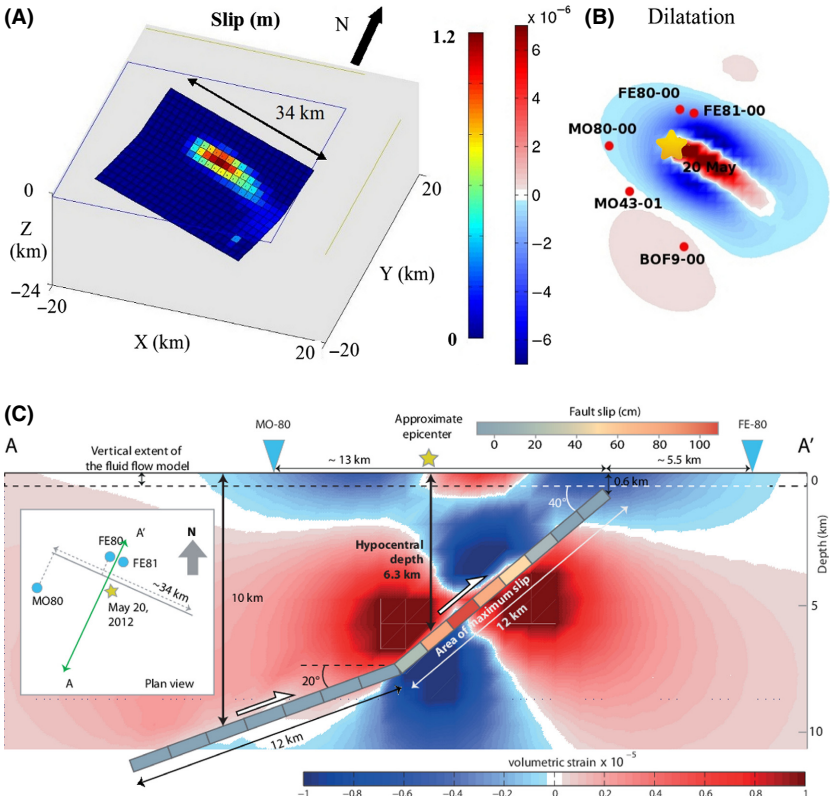

Fig. 3. (A) Fault model of the May 20 earthquake, based on the inversion of GPS and InSAR data (after Pezzo *et al.* 2013). Color represents the slip, which varies from 0 (blue) to a maximum of 1.2 m (red). (B) Volumetric strain at the surface computed for the May 20 earthquake. Computed strain ranges from -6×10^{-6} to 24×10^{-6}. Red dots represent the wells, and the yellow star represents the epicenter of the May 20, 2012 event. (C) Spatial relations between the inferred fault, slip distribution and water wells in the area. Panel (C) highlights the different depths at which volumetric strain and fluid flow are computed.

or a change in water temperature or salinity (Marcaccio & Martinelli 2012). The temporal evolution of water-level changes is shown in Fig. 2 for the period from May 13 to June 17, 2012. The first measurement after the earthquake on May 20, took place about 1 h after the event (5:00 AM, local time).

The northernmost wells (FE80-00 and FE81-00) are both shallow (−40 m) and less than 3 km apart; their evolution is similar: water level undergoes an instantaneous increment (0.2 and 0.5 m, respectively) after the first earthquake. Then the water level quickly drops, but doesn't recover its pre-earthquake elevation in the time span considered in this work. After the main peak, both these wells feature a second peak (labeled *r* in Fig. 2A,B), lasting a couple of days, unrelated to seismicity, that is not recorded in the other, deeper wells. Finally, a last peak, equally sharp but of lower magnitude, corresponds to the second mainshock, on May 29, and is again followed by a slow decay. Greater changes are observed in the deepest well (MO80-00, 300 m), where the May 20 earthquake caused an instantaneous water-level rise of 1.6 m, followed by a slow, partial recovery (Fig. 2C). Similar behavior is observed after the May 29 event, when the peak is followed by a slightly slower decline. More than 3 months were necessary in this case to restore the original water level. Water-level variations are also recorded at wells MO43-01 and BOF9-00 (Fig. 2D,E). Both these wells, however, undergo heavy withdrawal associated with nearby industrial activities that were disrupted by the earthquake. These fluctuations are much larger than the observed coseismic effect, which is only clearly visible in MO43-01 at the time of the second shock. A gradual water-level rise in BOF9-00 is observed only one day after the May 20 event and does not seem to be related to seismicity.

As precise information on water withdrawal is not available, data from these wells are not considered hereafter. In the following, we focus on some specific features of the observed water-level evolution: (i) the differences in water-level change between the shallow and deep wells; (ii) the change in the decay rate during the postseismic stage; (iii) the residual level rise that characterizes the shallow wells after the May 20 earthquake; (iv) the minor water-level change observed in the shallow wells 2 days after the earthquake. At this time, we limit our study to the effects associated with the mainshock of May 20, 2012.

MODELING THE WATER RESPONSE

Representing the earthquake

In this work, we assume that the water-level change is triggered by stress transfer from the rock to the pore fluid caused by the deformation of the matrix skeleton (Ge &

Stover 2000; Jónsson *et al.* 2003). Such stress transfer translates into a pressure change that can drive fluid motion. To describe this effect for the May 20 mainshock, we consider the fault model (in terms of coseismic slip distribution and fault geometry) described by Pezzo *et al.* (2013) and calculate the volumetric strain change induced by the seismic event in a homogeneous, elastic half-space (Okada 1992; Nostro *et al.* 1998). The volumetric strain change is computed at different locations (every 2 km) within a radius of 110 km from the epicentral area and from the ground surface to a maximum depth of 10 km (Fig. 3C). At the well location, the distribution of volumetric strain was computed along intersecting vertical planes, to gain a detailed picture of the spatial distribution of the deformation**.** Figure 3 shows that positive volumetric strain is induced at hypocentral depth while above a depth of about 2 km negative strain is induced, driving the observed pore pressure increase.

We choose an average Poisson ratio $\nu = 0.3$ typical of sandstone in undrained conditions (Rice & Cleary 1976) to represent the rock properties of the shallow crust. The resulting volumetric strain change ($\Delta\varepsilon_{kk}$) at the surface is shown in Fig. 3B and ranges from -6×10^{-6} (contraction, in blue) to 24×10^{-6} (expansion, in red). The largest changes occur within a few km from the epicenter. All the considered wells are located in an area of contraction. This volumetric strain change is considered as approximately constant within the fluid flow domain (Fig. 3C). The computed volumetric strain was used to calculate the corresponding isotropic stress change, in the undrained limit, as $\Delta\sigma_{kk} = 3Ku \cdot \Delta\varepsilon_{kk}$, where $\Delta\sigma_{kk}$ is the trace of the stress tensor change and K_u is the undrained bulk modulus. Seismic tomography and stratigraphic data (Cocco *et al.* 2001 and ref. therein) for this region show an important structural discontinuity at a depth of 130 m, where shear wave velocity changes by a factor of 5 (from 400 to 2000 m/s). Based on this evidence, we considered different elastic properties above and below this depth, computing the rigidity as $\mu = Vs^2 \cdot \rho$ where Vs is the shear wave velocity and ρ is the rock density (see Table 1). From the expression $K_u = \frac{2}{3}\mu(1+\nu)/(1-2\nu)$, where μ is the rigidity and υ is the undrained Poisson modulus (Table 1), we obtained different values of K_u above and below 130 m depth. Accordingly isotropic stress changes, unlike volumetric strain changes, can be considered as depth dependent, basically due to rigidity variations with depth. Then, two maps of isotropic stress change were considered above and below the depth of 130 m. To evaluate the groundwater response, these stress changes are translated into pore pressure variations. The linear theory of poroelasticity describes how the stress change is transferred from the solid skeleton to the pore fluid, according to a simple relation (Skempton 1954; Roeloffs 1996; Roeloffs & Quilty 1996; Grecksch *et al.* 1999; Ge & Stover 2000):

Table 1 Elastic parameters used to calculate the two stress maps, above and below the depth of 130 m. μ = rock rigidity; Vs = shear wave velocity; ν = undrained Poisson modulus; ρ = rock density. Poisson ratios are taken from Mavko *et al.* 2003.

	Shallow layers	Deep layers
μ (GPa)	0.4	9.6
Vs (m s^{-1})	400	2000
ν	0.4	0.37
ρ (kg m^{-3})	2300	2400

$$\Delta P = -B\Delta\sigma_{kk}/3 \quad (1)$$

where P is the pore pressure and B is the Skempton's coefficient (we assumed $B = 1$ to represent sediments of the Po Plain). Eq. (1) is valid in undrained conditions. In our case, the pressure change caused by the earthquake can be considered instantaneous compared to the time required by the water to flow through the porous rocks, hence the assumption of undrained conditions is justified.

Equation (1) was applied to compute the perturbation caused by the May 20 earthquake in all the grid blocks of the computational domain below the water table (i.e., water saturated). Figure 4 shows the resulting pressure changes that we applied to all the computational grid blocks above −130 m (a), and below such depth (b). The resulting pressure distributions were applied as initial conditions in the porous media flow model described below. The locations of the shallow and deep well considered in the transient evolution are also indicated in Fig. 4 (black squares).

Representing the aquifer response

The aquifer response to the computed pressure perturbation is studied with the TOUGH2 simulator, which can describe flow of water through saturated and unsaturated porous media (Pruess *et al.* 2012). The model is based on an integrated finite difference approach with a first-order, fully implicit time discretization. Our application describes the coupled flow of heat, water, and air through a heterogeneous porous matrix, accounting for phase interference and for capillary pressure effects when air and liquid water coexist. In our application, we neglect chemical reactions and deformation of the porous medium. Our study area is represented with a three dimensional computational domain discretized with 41600 elements ($20 \times 20 \times 104$) for a total length and width of 100 km, and 0.5 km depth. The computational mesh is particularly fine in the vertical dimension, to capture small changes in water level: element thickness ranges from 1 to 80 m, with greater resolution near the surface. To keep the number of grid blocks to a manageable level, the mesh is coarser in the horizontal dimensions, where elements size ranges from 4×4 km,

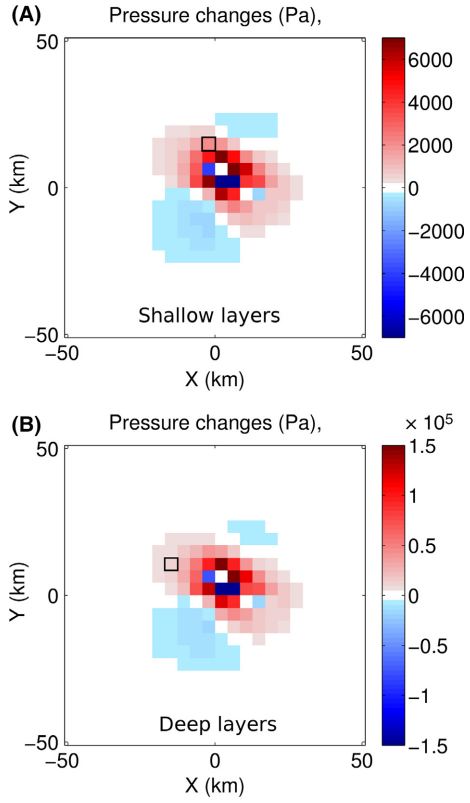

Fig. 4. Distribution of pore pressure change (Pa) due to the May 20 earthquake along a horizontal section of the computational domain (100 × 100 km). (A) Values assigned at depth less than 130 m. The same pressure change is applied along the vertical direction for grid blocks of layers 1 and 2. (B) Values assigned at depths greater than 130 m. The same pressure change is applied along the vertical direction for all the grid block of layers 3 and 4. Squares represent the computational grid block elements. Black squares highlight the grid block corresponding to the shallow (A) and deep wells (B). Note the change in color scale.

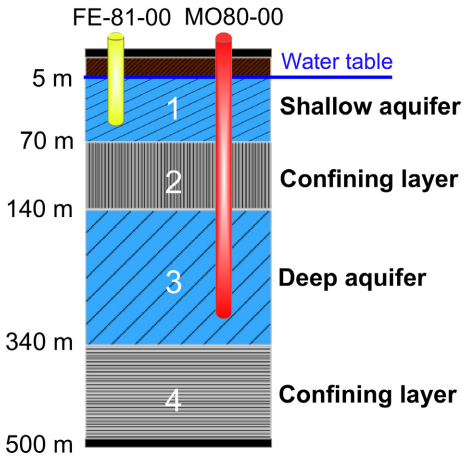

Fig. 5. Layering assigned to the porous media flow model. Layers 1 and 3 represent two aquifers, layers 2 and 4 are two confining layers. The domain is entirely water saturated from the bottom to the elevation of the water table (5 m below the surface). The shallow and deep wells, representing FE-81-00 and MO80-00 water wells, respectively, are shown.

near the fault location, to a maximum area of 12 × 12 km. We performed several grid tests (Figs S2–S5) to ensure that the extreme aspect ratio of the elements does not introduce a significant bias in the estimate of water-level change.

The stratigraphy of the region is well constrained because of the availability of a large number of data derived from deep and shallow drilling and from geophysical prospecting (Cocco *et al.* 2001). The shallower portion of the Po Plain is characterized by several superimposed aquifers that are interspersed with impervious units, resulting from the alternating sedimentation of clay and sand (Regione Emilia-Romagna and ENI-AGIP, 1998; Marcaccio & Martinelli 2012). To represent this general setting, we implement a general shallow stratigraphy where two aquifers are separated by less permeable layers that we will consider here as confining units (Fig. 5). In this stratigraphy, an upper aquifer (1) overlies a low-permeability layer (2). The deep aquifer (3) is confined by two confining units (2 and 4). To represent the hydraulic properties of such a stratigraphic setting we choose reasonable parameter ranges that represent the average response of laterally extensive aquifers and impervious layers. We tested several combinations of porosity and permeability in the four layers we present here a set of results (Table 2). All the considered values are within the characteristic range of fine sands and layered clays that compose the shallow sequence of the Po plain (Bordoni *et al.* 2012; Priolo *et al.* 2012).

The unsaturated layer is 5 m thick, while below this depth the porous medium is fully water saturated. We apply a geothermal gradient of 40°C km^{-1} and let the model compute the hydrostatic pressure distribution at steady state. The upper and lateral boundaries are open to heat and fluid flow. This condition is implemented in TOUGH2 by imposing fixed conditions to all the elements along the boundaries. The upper boundary is therefore at atmospheric condition (air saturated, 0.1 MPa and 20°C), and the elements along vertical boundaries are set at the temperature, pressure, and water saturation corresponding to their depth in hydrostatic conditions. The bottom boundary is closed to heat and fluid flow. This condition corresponds to a shallow system that is effectively insulated by the presence of an impervious layer. The presence of such a layer is consistent with the geological setting of the area, characterized by multiple superimposed aquifers associated with alternating layers of sand and clay (Ori 1993; Amorosi *et al.* 1996; Regione Emilia-Romagna and ENI-AGIP, 1998). The observed lack of temperature and/or salinity changes in monitored wells, also confirms the relative insulation of the shallow aquifer with respect to warm saline fluids from greater depths (Marcaccio & Martinelli 2012). The imposition of a very shallow bottom boundary

Table 2 Rock porosity and permeability values assigned to the layers in the four cases. Permeability is isotropic.

Layer	Porosity All cases	Permeability (m^2) Case 1	Case 2	Case 3	Case 4
1	0.4	1.5×10^{-13}	1.5×10^{-13}	1.5×10^{-14}	3.0×10^{-14}
2	0.4	1.5×10^{-15}	1.5×10^{-14}	1.5×10^{-16}	1.5×10^{-15}
3	0.3	1.5×10^{-13}	1.5×10^{-13}	1.5×10^{-14}	1.5×10^{-13}
4	0.4	1.5×10^{-15}	1.5×10^{-14}	1.5×10^{-16}	1.5×10^{-15}

stems from the lack of monitoring data at greater depths and from the need to ensure enough resolution with a manageable number of elements in the computational domain. The use of a shallow computational domain is appropriate in our case, as we are interested in the short-term evolution (weeks) of shallow wells. Taking into account the diffusion equation governing pore pressure, the time scales needed to detect effects related to pore pressure changes near the hypocenter (6 km depth) are expected to be much longer than weeks, due to the long distance L (>6 km) and the lower hydraulic diffusivity D expected at increasing depths (the diffusion time scales as L^2/D). A test (not shown) performed with a deeper domain (700 m) confirmed that the depth of the impervious boundary does not significantly affect the results.

The seismically induced pressure changes (Fig. 4) are then applied at the beginning of each simulation, and the model is run to describe the system evolution during the following 20 days.

SIMULATION RESULTS

Four permeability structures are considered in detail (Table 2). Case 1 assumes a large permeability contrast between the aquifers and the confining layers and a relatively high permeability for the aquifers. Figure 6 shows the pressure distribution at different depths (−40 and −300 m, corresponding to the depths of the wells) and at different times (initially and after 1 day).

The shallow aquifer is characterized by lower pore pressure perturbations and by a faster evolution than the deep aquifer: after 1 day of simulation, pore pressure has almost returned to its initial unperturbed value, whereas the deep aquifer is still perturbed. After 20 days of simulation the pore pressure is back to hydrostatic equilibrium everywhere (not shown).

The temporal evolution of pore pressure in the deep and shallow wells is shown Fig. 7, which compares results obtained with different permeability distributions (Table 2).

In the shallow wells (Fig. 7A), when the earthquake strikes, the pressure undergoes an instantaneous increase of about 3 kPa from the initial, unperturbed value. The corresponding piezometric head variation ($\Delta h = \Delta P/\rho g$) is of the order of 30 cm, in good agreement with the observations. Subsequent evolution is characterized by a quick pressure drop, followed by a second and lower pressure increment. This second pressure fluctuation reflects the arrival of fluids from the deeper region of the domain that were set in motion by the earthquake, at the beginning of the simulation. The rate and amplitude of this second pressure fluctuation depends on the permeability assigned to both the aquifers and the confining layers. In Case 1 and 3, this pressure rise occurs after about 1 day of simulation, while the strongest and fastest response is obtained in Case 2, where all layers are rather permeable and the second pressure pulse occurs right after the coseismic one. This is the only simulation where pressure fully recovers to its initial, unperturbed value in the simulated 20 days. In all other cases, the pressure in the shallow aquifer remains above its initial value.

In the Case 3, the water-level drop that occurs soon after the earthquake is slower than those in Case 1 and Case 2 mainly due to the lower permeability of the shallow aquifer. In this case, the arrival of fluids from the deep aquifer has little influence on the well pressure and occurs after 5 days. The pressure evolution obtained in Case 4 better resembles the observed well behavior, with a second, minor level rise after the coseismic peak, followed by a very slow recovery to pre-earthquake values. Pressure evolution in the deep, confined well is characterized by greater changes and by a slower postseismic evolution (Fig. 7B). In our calculation, the earthquake causes a pore pressure increase of about 14 kPa. This corresponds to a water-level change of 1.4 m, similar to the actual observation (1.6 m). In this case, the impervious bottom boundary prevents outflow of fluids toward deeper layers, and postseismic pressure evolution is characterized by a monotonic decay, whose rate depends on the permeability structure. As with the shallow wells, the more permeable system (Case 2) is the only one where pressure returns to its initial value within the 20 days of our simulation. In this case, the pressure evolution obtained in Cases 1 and 4 better reflect the rate of water-level decay observed in the deep wells. Notwithstanding the applied geothermal gradient (40°C km^{-1}), and even though the two aquifers are separated by a rather permeable confining layer, the upward component of fluid flow does not provides a measurable increase of water temperature, as observed.

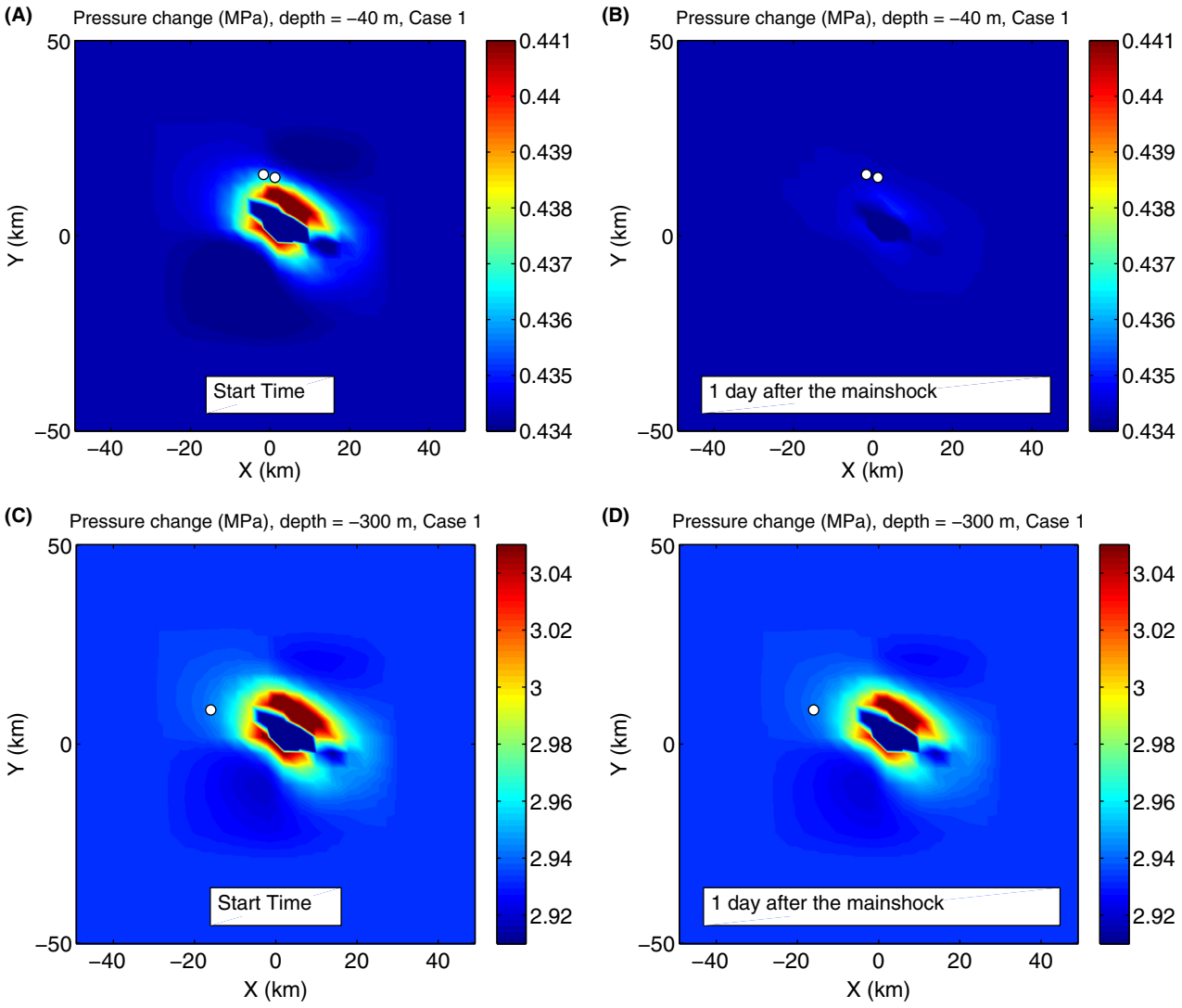

Fig. 6. Case 1. Simulated pressure distribution (MPa) on a horizontal section, at different depths and times: shallow wells depth (−40 m), at the beginning of the simulation (A) and after 1 day (B). Deep well depth (−400 m), at the beginning of the simulation (C) and after 1 day (D). White dots represent the water wells. Note the change in color scale.

COMPACTION AND METEORIC RECHARGE

Numerical simulations provide information on pressure evolution that can be easily converted into water-level changes, allowing comparison with observations from deep and shallow wells (Fig. 8). The observed water-level changes are compared with Case 4, which provides the better match with the data. Figure 8 also shows results obtained accounting for two different effects that may have affected the observed water level: meteoric recharge and compaction.

The May 20 event was followed by two rainy days. The weather monitoring stations in the area measured 30 to 45 mm of rain accumulated from May 20 to May 22 (Table S2 data avaiable by Arpa Emilia-Romagna - http://www.arpa.emr.it). The effects of rain may appear with a large time delay in deep aquifers (Roeloffs 1998), but groundwater bodies at shallow depths are quickly influenced by meteoric recharge (Marcaccio & Martinelli 2012). The effect of rain was incorporated into our simulations by placing water sources along the top of the domain. The water sources inject water at ambient temperature (20°C) and at constant rate of 2.6×10^{-4} kg m^{-2}s, from May 20 (12:00 AM) to May 22 (12:00 AM), corresponding to about 45 mm of cumulative rainfall. Meteoric recharge makes the second peak sharper and higher, but does not affect the rate of water-level decline in the long term (Fig. 8A).

The second effect we introduced is related to coseismic changes of hydraulic properties. Seismic shaking can affect

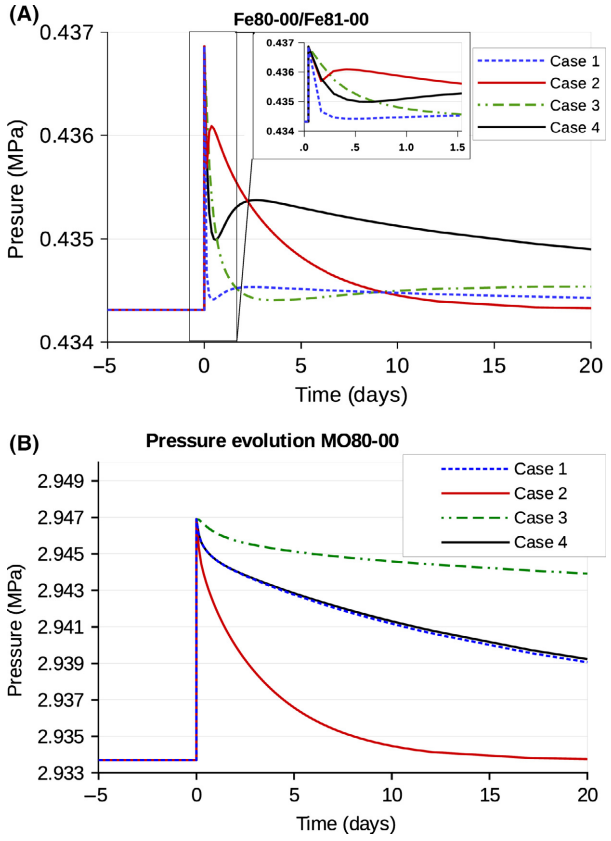

Fig. 7. Bottom hole pore pressure transient evolution (MPa) for (A) the shallow wells (FE80-00 and FE81-00), and (B) the deep well MO80-00, for the four different permeability distributions given in Table 2.

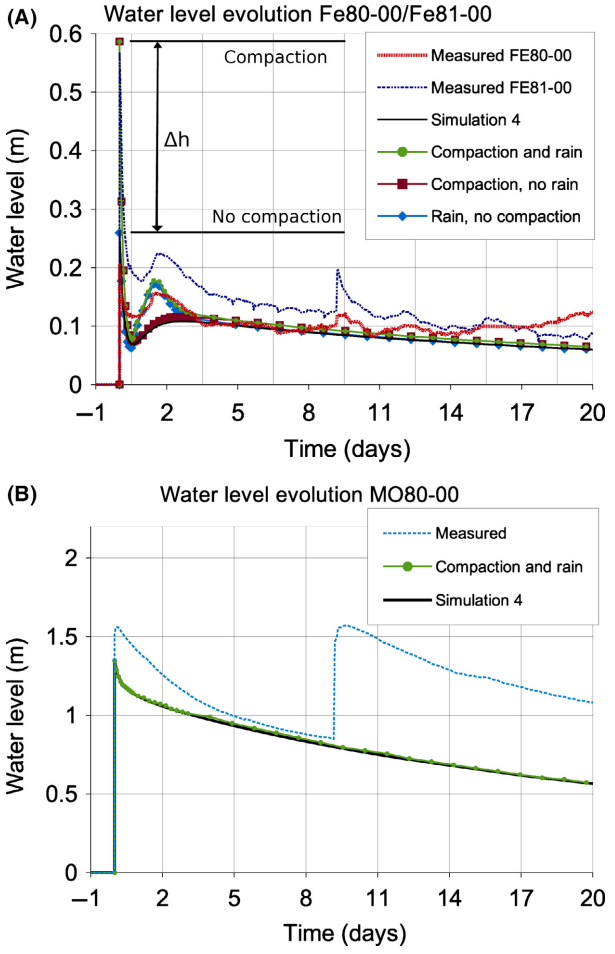

Fig. 8. Water-level changes (m) for (A) the shallow wells (FE80-00 and FE81-00), and (B) the deep well (MO80-00) for case 4. Simulations results obtained with and without compaction and rain are compared with observed evolution.

the size, distribution, and connectivity of pores and thus change both porosity and permeability (Wang *et al.* 2001; Manga & Wang 2007; Convertito *et al.* 2013). In an alluvial plain, like the Po Plain, ground shaking may cause the re-arrangement of solid grains (especially where unconsolidated sediments are present under low confining pressures), favoring compaction and associated porosity and permeability decreases. In our case, the shallow layer is made of alternating silt and clay and is expected to be highly susceptible to compaction. We assume that earthquake shaking instantaneously caused a permanent reduction of the porosity in the shallow aquifer only, from the initial, unperturbed value Φ_0, to a new, lower value $\Phi_1 = \Phi_0 - \Delta\Phi$. We tested different values of $\Delta\Phi$ and here present results obtained with $\Delta\Phi = 2 \times 10^{-3}$. The porosity loss causes an increase (Δh^1) of the initial water level h_0 corresponding to $\Delta h^1 = h_0 \cdot \Delta\Phi/\Phi_1$. A corresponding pressure change $\Delta P = \rho g \Delta h^1$ is assigned to all computational cells in the shallow aquifer. For a porosity loss of 2×10^{-3}, the resulting water-level change is of the order of 30 cm and corresponds to a pore pressure increment of about 3 kPa. Compaction also affects permeability and the expected change is computed as a function of the porosity changes, according to the equation $\boldsymbol{k_1} = k_0 \ (\boldsymbol{\Phi_1}/\Phi_0)^{\alpha}$ (David *et al.* 1994; Chin *et al.* 2001; Rinaldi *et al.* 2014), where k_1 is the new permeability after compaction, k_0 is the initial permeability (Table 2, Case 4), and α is the so-called porosity sensitivity, whose value ranges from 1.86 to 25.4 in sandstones (Yale 1984; David *et al.* 1994). Again we performed several tests and the best results were achieved using $\alpha = 15$. The simulations that include meteoric recharge and compaction better capture some details of the shallow wells evolution: accounting for compaction doubles the initial water-level rise, leading to a maximum value of 0.59 m. Once the pressure drops, both simulations, with and without compaction, exhibit similar behavior in the long term (Fig. 8A). Introduction of meteoric recharge results in a second pressure peak that nicely matches the water-level rise observed 2 days after the seismic events. Long-term evolution is not affected by the rainy days. Rain and compaction do not affect the water level in the deep well (Fig. 8B). The simulated rain event

is too small to affect the deep aquifer, which is effectively confined by layer 2. This is consistent with the available data, suggesting that the recharge area of the deep aquifer is located more than 30 km south of the study area, on the edge of the Apennines chain (Regione Emilia-Romagna and ENI-AGIP, 1998).

DISCUSSION & CONCLUSIONS

The May 20, 2012 Emilia earthquake caused a increase in water level recorded both in deep and shallow water wells. The deep and shallow wells display remarkable differences both in the magnitude of the observed changes and in the rate of recovery. Our approach combines a description of the seismic source, in terms of fault geometry and coseismic slip distribution, based on the inversion of GPS and InSAR coseismic displacements, with a specific porous media flow model that enables us to account for the complexities of a heterogeneous stratigraphy. Our results show that the effects of the earthquake can be suitably represented in the fluid flow model as an instantaneous variation of pore pressure, whose magnitude and location depend on the slip distribution along the fault. The pore pressure change experienced in each well depends on well depth and position with respect to the epicenter. The properties of the hydrogeologic units control the postseismic dissipation of this pressure pulse: the shallow, unconfined aquifer is characterized by a very fast evolution that dissipates most of the coseismic pressure pulse within a few days, while the deep, confined aquifer requires a longer recovery time. Our simulations capture the different orders of magnitude that characterizes the response of deep and shallow wells to the same seismic event. The results presented above suggest that the observed water-level changes depend not only on the magnitude and location of the seismic event, but also on the presence and properties of heterogeneous materials. The observed evolution is well represented assuming a very permeable (1.5×10^{-13} m^2) aquifer at depth, well-confined by two low-permeability (1.5×10^{-15} m^2) layers, and overline by a slightly less permeable (3×10^{-14} m^2) unconfined aquifer. The absence of full recovery of previous water levels in the shallow wells (FE80-00 and FE81-00) is well explained by pressure evolution in a groundwater system with a deep aquifer confined between low-permeability layers. Coseismic compaction and two rainy days explain the details of the water-level changes. Different degrees of compaction could explain the different water levels recorded by the two wells that are very close in space. Episodes of liquefaction and spontaneous fluid emissions have been reported in the aftermath of the earthquake and suggest that significant changes in the rock properties (including compaction) occurred at very shallow depth (Emergeo Working Group, 2012, http://emergeo.ingv.it). The occurrence of shallow compaction is also consistent with the observed response of these wells to the second earthquake, on May 29 (Fig. 2A,B). Although we did not simulate this second event, we highlight the smaller water-level changes associated with this event and the slower (and complete) recovery to pre-earthquake levels. If the lower amplitude of the water-level rise is due to a greater distance from the epicenter, the slower recovery suggests a lower aquifer permeability, consistent with compaction.

The deep well (MO80-00) is characterized by simpler evolution that is not affected by rain or shallow compaction. Its response to the May 29 event equals the water-level rise observed on May 20 (although the epicenter of the second event is closer) and is followed by a slightly slower recovery. Numerical simulations provide a good description of the overall behavior, but fail to reproduce details of the coseismic water-level change. This lack of correspondence may be due to a poor choice of local rock properties (both elastic and hydraulic), in a geological setting characterized by strong lateral heterogeneities. Short-term pressure changes inside the well are very sensitive to the local ground properties. On the contrary, the long-term evolution depends on larger spatial scales, and a general description with average material properties is better suited to obtain a good match with data. Future development should extend the study to hypocentral depths to account for the fluid migration within seismogenic areas and investigate the role of fluid flow in the evolution of the seismic sequence.

ACKNOWLEDGEMENT

We wish to thank the anonymous reviewers whose comments and suggestions greatly improved our work.

REFERENCES

Amorosi A, Farina M, Severi P, Preti D, Caporale L, Di Dio G (1996) Genetically related alluvial deposits across active fault zones: an example of alluvial fan-terrace correlation from the upper Quaternary of the southern Po Basin, Italy. *Sedimentary Geology*, **102**, 275–95.

Bordoni P, Azzara R, Cara F, Cogliano R, Cultrera G, Di Giulio G, Fodarella A, Milana G, Pucillo S, Riccio G, Rovelli A, Augliera P, Luzi L, Lovati S, Massa M, Pacor F, Puglia R, Ameri G (2012) Preliminary results from EMERSITO, a rapid response network for site-effect studies. *Annals of Geophysics*, **55**, 599–607.

Brodsky EE, Roeloffs E, Woodcock D, Gall I, Manga M (2003) A mechanism for sustained groundwater pressure changes induced by distant earthquakes. *Journal of Geophysical Research*, **108**, 2390 doi:10.1029/2002JB002321.

Cesca S, Braun T, Maccaferri F, Passarelli L, Rivalta E, Dahm T (2013) Source modelling of the M5–6 Emilia-Romagna, Italy, earthquakes (2012 May 20–29). *Geophysical Journal International*, **193**, 1658–72 doi:10.1093/gji/ggt069.

Chin LY, Raghavan R, Thomas LK (2001) Fully-coupled geomechanics and fluid-flow analysis of wells with stress-dependent permeability. *SPE J*, **5**, 32–45.

Cocco M, Ardizzoni F, Azzara R, Dall'Olio L, Delladio A, Di Bona M, Malagnini L, Margheriti L, Nardi A (2001) Broadband waveforms and site effects at a borehole seismometer in the Po alluvial basin (Italy). *Annals of Geophysics*, **44**, 137–54.

Convertito V, Catalli F, Emolo A (2013) Combining stress transfer and source directivity: the case of the 2012 Emilia seismic sequence. *Scientific Reports*, **3**, 3114.

David C, Wong T-F, Zhu W, Zhang J (1994) Laboratory measurements of compaction-induced permeability change in porous rocks: implication for generation and maintenance of pore pressure excess in the crust. *Pure and Applied Geophysics*, **143**, 425–56.

Elkhoury JE, Brodsky EE, Agnew DC (2006) Seismic waves increase permeability. *Nature*, **441**, 1135–8.

Ellsworth WL (2013) Injection-induced earthquakes. *Science*, **341**, 142.

Emergeo Working Group (2012) Technologies and new approaches used by the INGV EMERGEO Working Group for real-time data sourcing and processing during the Emilia Romagna (northern Italy) 2012 earthquake sequence, Annals of Geophysics, **55**, 689–95.

Ge S, Stover SC (2000) Hydrodynamic response to strike- and dip-slip faulting in a half-space. *Journal of Geophysical Research*, **105**, 25513–24.

Grecksch G, Roth F, Kümpel HJ (1999) Coseismic well-level changes due to the 1992 Roermond earthquake compared to static deformation of half-space solutions. *Geophysical Journal International*, **138**, 470–8.

Grünthal G (2013) Induced seismicity related to geothermal projects versus natural tectonic earthquakes and other types of induced seismic events in Central Europe. *Geothermics*, **52**, 22–35.

Jónsson S, Segall P, Pedersen R, Björnsson G (2003) Post-earthquake ground movements correlated to pore-pressure transients. *Nature*, **424**, 179–83.

Manga M, Brodsky EE (2006) Seismic triggering of eruptions in the far field: volcanoes and geysers. *Annual Reviews of Earth and Planetary Sciences*, **34**, 263–91.

Manga M, Wang CY (2007) Earthquake hydrology. *Treatise of Geophysics*, **4**, 305–28.

Manga M, Brumm M, Rudolph ML (2009) Earthquake triggering of mud volcanoes. *Marine and Petroleum Geology*, **26**, 1785–98.

Manga M, Beresnev I, Brodsky EE, Elkhoury JE, Elsworth D, Ingebritsen S, Mays DC, Wang CY (2012) Changes in permeability by transient stresses: field observations, experiments and mechanisms. *Reviews of Geophysics*, **50**, RG2004.

Marcaccio M, Martinelli G (2012) Effects on the groundwater levels of the May-June 2012 Emilia seismic sequence. *Annals of Geophysics*, **55**, 4.

Mavko G, Mukerji T, Dvorkin J (2003) *The Rock Physics Handbook: Tools for Seismic Analysis of Porous Media*. Cambridge University Press, Cambridge.

Miller SA, Collettini C, Chiaraluce L, Cocco M, Barchi M, Kaus BJP (2004) Aftershocks driven by a high-pressure CO_2 source at depth. *Nature*, **427**, 724–7.

Nostro C, Stein RS, Cocco M, Belardinelli ME, Marzocchi W (1998) Two-way coupling between Vesuvius eruptions and southern Apennine earthquakes, Italy, by elastic stress transfer. *Journal of Geophysical Research*, **103**, 24487–504.

Okada Y (1992) Internal deformation due to shear and tensile faults in a half-space. *Bulletin of the Seismological Society of America*, **82**, 1018–40.

Ori GG (1993) Continental depositional systems of the Quaternary of the Po Plain (northern Italy). *Sedimentary Geology*, **83**, 1–14.

Pezzo G, Boncori JPM, Tolomei C, Salvi S, Atzori S, Antonioli A, Trasatti E, Novali F, Serpelloni E, Candela L, Giuliani R (2013) Coseismic deformation and source modeling of the May 2012 Emilia (Northern Italy). *Seismological Research Letters*, **84**, 645–55.

Priolo E, Romanelli M, Barnaba C, Mucciarelli M, Laurenzano G, Dall'Olio L, Abu Zeid N, Caputo R, Santarato G, Vignola L, Lizza C, Di Bartolomeo P (2012) The Ferrara thrust earthquakes of May-June 2012: preliminary site response analysis at the sites of the OGS temporary network. *Annals of Geophysics*, **55**, 591–7.

Pruess K, Oldenburg C, Moridis G (2012) TOUGH2 User's Guide, Version 2.1, Report LBNL-43134, Lawrence Berkeley National Laboratory, Berkeley, Calif.

Regione Emilia-Romagna and ENI-AGIP (1998) *Riserve idriche sotterranee della Regione Emilia Romagna*. S.EL.CA, Firenze, 119 pp.

Rice JR, Cleary MP (1976) Some basic stress diffusion solutions for fluid-saturated elastic porous media with compressible constituents. *Reviews of Geophysics*, **14**, 227–41.

Rinaldi AP, Rutqvist J, Cappa F (2014) Geomechanical effects on CO_2 leakage through fault zone during large-scale underground injection. *International Journal of Greenhouse and Gas Control*, **20**, 117–31.

Roeloffs EA (1996) Poroelastic techniques in the study of earthquake-related hydrologic phenomena. *Advances in Geophysics*, **37**, 135–95.

Roeloffs EA (1998) Persistent water level changes in a well near Parkfield, California, due to local and distant earthquakes. *Journal of Geophysical Research: Solid Earth (1978–2012)*, **103**, 869–89.

Roeloffs EA, Quilty EG (1996) Water level and strain changes preceding and following the August 4, 1985 Kettleman Hills, California, earthquake. *Pure and Applied Geophysics*, **149**, 21–60.

Scognamiglio L, Margheriti L, Mele F, Tinti E, Bono A, De Gori P, Lauciani V, Lucente F, Mandiello A, Marcocci C, Mazza S, Pintore S, Quintiliani M (2012) The 2012 Pianura Padana Emiliana seimic sequence: locations, moment tensors and magnitudes. *Annals of Geophysics*, **55**, 549–59.

Serpelloni E, Anderlini L, Avallone A, Cannelli V, Cavaliere A, Cheloni D, D'Ambrosio C, D'Anastasio E, Esposito A, Pietrantonio G, Pisani AR, Anzidei M, Cecere G, D'Agostino N, Del Mese S, Devoti R, Galvani A, Massucci A, Melini D, Riguzzi F, Selvaggi G, Sepe V (2012) GPS observations of coseismic deformation following the May 20 and 29, 2012, Emilia seismic events (northern Italy): data, analysis and preliminary models. *Annals of Geophysics*, **55**, 4.

Shi Z, Wang G, Wang CY, Manga M, Liu C (2014) Comparison of hydrological responses to the Wenchuan and Lushan earthquakes. *Earth and Planetary Science Letters*, **391**, 193–200.

Skempton AW (1954) The pore-pressure coefficients A and B. *Géotechnique*, **4**, 143–7 doi:10.1680/geot.1954.4.4.143.

Wang CY, Chia Y (2008) Mechanism of water level changes during earthquakes: near field versus intermediate field. *Geophysical Research*, **35**, L12402.

Wang CY, Manga M (2010) Hydrologic responses to earthquakes and a general metric. *Geofluids*, **10**, 206–16.

Wang CY, Cheng L-H, Chin CV, Yu SB (2001) Coseismic hydrologic response of an alluvial fan to the 1999 Chi-Chi earthquake, Taiwan. *Geology*, **29**, 831–4.

Wang Z, Fukao Y, Pei S (2009) Structural control of rupturing of the Mw7.9 2008 Wenchuan Earthquake, China. *Earth and Planetary Science Letters*, **279**, 131–8.

Weingarten M, Ge S (2014) Insights into water level response to seismic waves: a 24 year high- fidelity record of global seismicity at Devils Hole. *Geophysical Research Letters*, **41**, 74–80.
Yale DP (1984) Network Modelling of Flow, Storage and Deformation in Porous Rocks. Ph.D. Thesis, Stanford University, Calif.

SUPPORTING INFORMATION

Additional Supporting Information may be found in the online version of this article:

Table S1. Depths, distances and coordinates of each well from the 20 May epicenter.

Table S2. Cumulative rainfall over three days, measured by weather stations in the area.

Figure S1. Maps of the Emilia-Romagna region.

Figure S2. Test on the extreme cells aspect ratio in the computational mesh.

Figure S3. (a) Pressure (Pa) evolution through time (days), $x = y = 0$; $z = -101$ m, (b) Pressure (Pa) distribution along the X axis (m), $z = -110$ m, after 2 days of simulation.

Figure S4. Test on spatial resolution of the computational mesh.

Figure S5. (a) Pressure (Pa) evolution through time (days), $x = y = 0$; $z = -550$ m. (b) Pressure (Pa) distribution along the X axis (m), $z = -550$ m, after 2 days of simulation.

GEOFLUIDS

Volume 16, Number 3, August 2016

ISSN 1468-8115

CONTENTS

WILEY Blackwell

Geofluids* is abstracted/indexed in *Chemical Abstracts

This journal is available online at Wiley Online Library. Visit onlinelibrary.wiley.com to search the articles and register for table of contents and e-mail alerts.